

Contents lists available at ScienceDirect

Powder Technology

journal homepage: www.elsevier.com/locate/powtec



Role of coprecipitation and calcination of precursors on phase homogeneity and electrochemical properties of battery active materials



Hongxu Dong, Anny Wang, Gary M. Koenig Jr*

Department of Chemical Engineering, University of Virginia, 102 Engineers Way, Charlottesville, VA 22904-4741, USA

ARTICLE INFO

Article history: Received 17 February 2018 Received in revised form 16 April 2018 Accepted 10 May 2018 Available online 26 May 2018

Keywords:
Li-ion batteries
Cathode materials
LiMn1.5Ni0.504
Coprecipitation
Calcination
Diffusion controlled solid reaction
Materials characterization

ABSTRACT

Coprecipitation has previously been demonstrated to produce diverse compositions of battery precursor particles, frequently under the assumption that the precipitation of transition metals from the solution results in advantages with regards to efficient homogeneous local mixing of transition metal cations within the solid particles. Such mixing is generally considered as an advantage relative to solid state reaction of solid powders with the equivalent starting stoichiometry; however, very few studies have attempted to quantitatively confirm the impact of this local mixing on the resulting final materials. The extent to which local mixing from coprecipitation facilitates the mass transport of transition metals during the calcination process, which would be expected to aid in producing well crystallized single-phase particles, is not clear. Herein, this study will systematically compare the phase purity and crystallinity of oxide powders comprised of a blend of transition metals that were produced from either physical mixture of single transition metal precursors or multicomponent precursors produced via coprecipitation from solution. These experiments provide quantitative support for the role that local mixing, achieved via precipitation, plays in forming high crystallinity final materials with the desired phase. LiMn_{1.5}Ni_{0.5}O₄ was used as a model multicomponent target final material after calcination.

© 2018 Elsevier B.V. All rights reserved.

1. Introduction

Multicomponent transition metal (TM) oxides are the most commonly used cathode active materials in lithium-ion (Li-ion) batteries due to their broad capabilities in power and energy densities that can be tuned depending on the transition metal stoichiometry [1–5]. Many techniques have been developed to synthesize multicomponent TM oxide materials at both research and industrial scales [6–11]. Solid state synthesis is straightforward in that single component powders of each element can be measured at the desired stoichiometry directly and then physically mixed, but high temperature and/or long calcination times are required due to large diffusion distances for ions to form homogeneous final active materials [12-14]. Sol-gel synthesis is a modified solid state method that achieves very good mixing of the constituent elements, but the control over particle morphology is relatively limited [15–18]. Spray pyrolysis, a synthesis route commonly utilized in industry, is very scalable and has local mixing homogeneity but also limited particle morphology control [19-21]. Coprecipitation is another popular method to synthesize precursors for multicomponent TM oxide materials. Mixing between different TMs is assumed to be achieved at the atomic level during coprecipitation reactions, which in principle will reduce the requirement for aggressive firing conditions.

E-mail addresses: hd5cw@virginia.edu (H. Dong), aw5nc@virginia.edu (A. Wang), gary.koenig@virginia.edu (G.M. Koenig).

The particle morphologies can be adjusted by tuning the reaction conditions and the particle morphologies can be well retained after the calcination process, which makes particle morphology control possible [22–25]. The method is fast, has low equipment needs, and is scalable. However, there are no reports on quantitative confirmation of the advantages of the assumed local mixing of precursors produced via coprecipitation, or to what extent the mixing facilitates ion diffusion during subsequent calcination. The focus of this study is to understand to what extent coprecipitation provides an advantage with local mixing of transition metals in the precursor particles, and for comparison we will also use solid state synthesis with physical mixing of single transition metal precursors.

LiMn_{1.5}Ni_{0.5}O₄ (LMNO) was chosen as the example final calcined material for this study. LMNO is commonly referred to as high voltage spinel due to its high redox potential at 4.7 V vs. Li/Li⁺ and because the material forms a spinel crystalline structure [1,26]. Depending on the distribution of Mn and Ni ions, LMNO may form two different crystallographic structures: the ordered P4₃32 space group and the disordered Fd-3 m space group [27]. Correct stoichiometry is essential for extracting the maximum capacity from LMNO materials. According to previous reports, either Mn or Ni enrichment relative to the target Mn:Ni 3:1 stoichiometry may cause decreased material capacity and/or material stability during electrochemical charge/discharge [17,26]. The sensitivity of electrochemical properties to stoichiometry necessitates good mixing between Mn and Ni ions in the final active material particles, since localized Mn or Ni segregation will result in phase

^{*} Corresponding author.

impurities and deteriorate resulting electrochemical properties of the materials. In this study, we will show the influence of local mixing and processing conditions on resulting final material crystal structure and electrochemical properties. The advantage of local mixing via coprecipitation relative to solid state physical blends of precursors is quantitatively characterized.

2. Materials and methods

2.1. Precursor synthesis and calcination

For the coprecipitation reaction, oxalate was used as the precipitation anion for all materials synthesized. Oxalate was chosen because Mn, Ni, and blends of Mn and Ni form stable oxalate dihydrates across the entire range of Mn:Ni ratios [17,28]. Other common precipitation anions, such as hydroxide and carbonate, have challenges with regards to impurity phases in the precipitate within certain stoichiometric ratios of Mn:Ni [10,24]. The dual functions of oxalate ions as both a precipitation reagent and a complexing agent also has the advantage of slowing down the precipitation rate which enables better control over the process within low concentration regimes [29].

The pure Mn and pure Ni TM precursors and the Mn:Ni 3:1 precursors were synthesized using coprecipitation via reaction of TM sulfate solutions with sodium oxalate solution. The synthesis was adapted from a procedure described previously [30]. In brief, a pre-determined amount of TM sulfate salts (containing either Mn, Ni, or Mn:Ni 3:1 feed) was dissolved in 400 mL deionized water (DI water) and heated to 60 °C. Separately, sodium oxalate was dissolved and heated to 60 °C in 400 mL DI water. The precipitation was initiated by pouring the TM sulfate solution into the sodium oxalate solution all at once with vigorous stirring. The solution was assumed to be homogeneous upon mixing, with the total concentrations of TM and oxalate both 0.15 M after the initial mixing step. The reaction was allowed to proceed for 30 min after mixing the two solutions together, at which time the precipitates were filtered and rinsed with DI water. The initial solution concentrations for TM and oxalate were chosen to mitigate the deviation of the precipitate composition relative to the feed conditions for the Mn:Ni 3:1 and to result in high yield of precursor particles [30]. The composition of the resulting precursor from the 3:1 Mn:Ni feed was determined by inductively coupled plasma – optical emission spectroscopy (ICP-OES, Perkin Elmer Optima 8000) to be Mn: Ni 2.82:1. As reported in the literature [31,32], the pure Ni, pure Mn, and 3:1 Mn:Ni precursors all were oxalate dihydrates as determined via thermal gravimetric analysis. After filtration and rinsing, all precursor material powders were dried in a vacuum oven at 80 °C overnight.

All precursor materials were calcined with a lithium salt to form lithium transition metal oxides. The obtained blend or pure precursor powders were mixed with 5% stoichiometric excess of LiOH for a target stoichiometric ratio of Li:TM 1.05:2. The mixing was conducted by hand using mortar and pestle for 10 min, and the mass of the powder for each batch of material mixed was kept around 3 g for consistency. The powder mixtures were then transferred into crucibles and put into a furnace (Carbolite CWF 1300 box furnace) and fired under an air atmosphere. All the calcination processes used 1 °C/min ramping rate for heating and the materials were held at the target top temperature for a specified period of time followed by naturally cooling down to room temperature. The top temperature and hold time were parameters that were varied and are specified in the manuscript text for a given material.

2.2. Materials characterization

Powder morphologies were characterized using a scanning electron microscope (SEM, FEI Quanta 650). Over 100 particles from SEM images were counted to determine the average particle size and standard deviation. The SEM was also equipped with energy-dispersive X-ray spectroscopy (EDS), which was used to identify elemental composition

and distribution in the particles. The crystal structure of precursors and calcined materials was determined using powder X-ray diffraction (XRD, PANalytical X'pert ProMPD). Thermal gravimetric analysis (TGA, TA Q50) was performed to determine the water stoichiometry in the precipitates and to locate the temperatures where decomposition processes occurred for the precursors. All the TGA tests were conducted in an air atmosphere with the ramping rate of 10 °C/min.

Electrochemical characterization of the final calcined active materials was conducted by using the calcined powders as the cathode active material in Li-ion battery cells paired with lithium metal anodes. The CR2032-type cells were fabricated with cathodes comprised of a blend of 80 wt% active materials, 10 wt% acetylene black, and 10 wt% polyvinylidene difluoride binder (dissolved in *N*-methyl-2-pyrrolidone). The electrode was cast from a slurry onto aluminum foil with a doctor blade set at a gap height of 250 µm. The electrode was first dried in air at 80 °C for 24 h, and then subsequently further dried under vacuum at 70 °C for 3 h. From the electrode foil, smaller disks with 1.6 cm² area were punched to be used as cathodes in the coin cells. The cells, with the composite cathodes paired with lithium metal foil anode, were assembled inside an argon-filled glove box with polymer trilayer membrane as separators and LiPF₆ dissolved in 3:7 vol% ethylene carbonate: ethyl methyl carbonate as the electrolyte. The cells were cycled within a voltage window of 3.6-4.9 V at room temperature using a MACCOR multichannel battery cycler. The cells were cycled galvanostatically at C/10, which corresponded to 14.67 mA g^{-1} of active material powder in the electrode, and the total charge/discharge current was adjusted by the amount of active material within a given electrode. The discharge profiles and dQ/dV profiles reported in this manuscript were from the fourth charge/discharge cycle, after the capacity stabilized from material structural activation during the first few cycles [33,34].

3. Results and discussion

3.1. Experimental results

Thermal gravimetrical analyses (TGA) were conducted on the pure manganese and nickel oxalates and the blend (3:1 Mn:Ni) oxalate. The TGA profiles can be found in the Supplementary Information, Fig. S1. Two peaks in differential mass loss were observed for all precursors, one at lower temperature corresponding to structural water loss, and a peak at higher temperature which resulted from decomposition of the oxalate structure during formation of oxide. Even with the fast ramping speed (10 °C/min) in TGA, the dehydration and decomposition processes were completed below 350 °C for all oxalate compounds. The melting point of LiOH is 450–471 °C from ICSC data (CAS #: 1310-66-3), thus above this temperature the liquid LiOH should obtain good contact and distribution with the resulting TM oxide particles. Based on the TM oxalate decomposition temperatures and LiOH melting temperature, we chose a lowest target calcination temperature of 500 °C. The highest calcination temperature was 850 °C, which was a common calcination temperature for similar materials and has been reported to result in good crystallinity while producing desirable primary particle size [14,33,35]. An intermediate calcination temperature of 700 °C was chosen because this temperature has been reported to promote formation of the ordered phase of LMNO [27,36]. The holding time at the target temperature of 700 °C was also varied to understand how the hold duration impacts the crystallinity of the product materials, with the extended hold being expected to facilitate more significant ion diffusion which could help to anneal out metastable phases and enable improved crystallinity. The product samples were named in the format of M-T-t, where M designates the mixing method which was either physically mixing of the two precursors (P, which stands for 'physical' mixing the two TMs) or coprecipitation of the blend TM solution (S, which stands for 'solution' mixing the TMs); T represents for the target top temperature in degrees Celsius, and t is the holding time at the target temperature in hours. For example, the sample referred to as S-5006 was obtained by calcining the coprecipitated precursor from the blend TM solution with LiOH at 500 °C for 6 h; whereas sample P-500-6 was obtained from calcining the physical mixture of the two pure TM precursors and LiOH at 500 °C for 6 h.

The manganese nickel blend oxalate (MnNiOx, chemical formula was Mn_{0.74}Ni_{0.26}C₂O₄·2H₂O from ICP and TGA) particles exhibit octahedral secondary particle morphologies and average particle size of 10.2 \pm 1.0 µm (Fig. 1a). Pure manganese oxalate (MnOx, chemical formula MnC₂O₄·2H₂O) precursors consisted of larger and more irregular particles, with overall particle dimensions of 24.0 \pm 1.9 μ m (Fig. 1b). The pure nickel oxalate (NiOx, chemical formula NiC₂O₄·2H₂O) precursors were aggregates of smaller primary particles, with secondary particle morphologies being roughly spherical with lengths of 3.6 \pm 0.7 μm (Fig. 1c). Significant aggregation of countable secondary particles can also be observed from the image. The SEM images of the solution mixed sample and physical mixed sample after firing with Li salt at 850 °C for 6 h (S-850-6 and P-850-6) are shown in Fig. 1d, e, respectively. It can be clearly seen from Fig. 1d the S-850-6 particles retained the secondary morphology of the precursor (Fig. 1a) after calcination. However, calcination resulted in the formation of nanometers-scale primary particles agglomerated together, with new pores that resulted from the escape of H₂O and CO₂ gases from the inner structure during decomposition of the oxalate and shrinkage of the structure from crystallization [37,38]. SEMs of the calcined physically mixed samples (Fig. 1e), resulting from calcination of a blend of the precursors shown in Fig. 1b, c revealed secondary morphologies consistent with the initial morphologies of both MnOx and NiOx precursors. The larger particles were consistent with the initial morphology of MnOx particles (Fig. 1b) and the smaller irregular shaped particles were consistent with NiOx particles (Fig. 1c). The segregation of secondary particles after calcination indicates poor intermixing during firing of the physical mixture. This clear segregation of particles appeared with all the physically mixed samples, and additional SEMs can be found in Supplementary information, Fig. S2.

For further evidence to support the impact of TM ion mixing in the precursor, EDS was performed on calcined oxides prepared using precursors that were either solution mixed or physically mixed, and the results can be found in Fig. 2. Fig. 2a shows the EDS elemental map of the solution mixed sample fired at 500 °C for 6 h (S-500-6) with Fig. 2b, c showing the individual maps of only Mn and Ni, respectively. Fig. 2d shows the EDS elemental maps of the physically mixed sample fired at 500 °C for 6 h (P-500-6) with Fig. 2e, f showing the individual maps of only Mn and Ni, respectively. As can be seen in the S-500-6 sample (Fig. 2a), Mn and Ni were evenly distributed in all the

particles in the image region. Any elemental segregation would be at a length scale that could not be observed in the SEM-EDS. Solution mixed samples fired at higher temperature also appeared homogeneous in EDS maps (data not shown). In contrast, the physically mixed P-500-6 sample image (Fig. 2d) had clearly segregated regions of Mn and Ni within the original particles and there was relatively low interdiffusion of TMs between constituent particles. The individual TM maps (Fig. 2e, f) show clear regions that are effectively pure Mn and pure Ni particles. Raising the calcination temperature and/or time did not significantly improve inter-diffusion level of TM ions observed in EDS (physically mixed samples fired at higher temperatures and longer times can be found in Supplementary Information, Fig. S3). In summary, EDS observations indicated there was significantly more inter-diffusion between Mn and Ni ions for samples with solution mixing compared to samples with physical mixing across all processing conditions. We do note that the physically mixed sample had more Mn and Ni interdiffusion at the highest firing temperature (P-850-6) relative to samples fired at lower temperatures (Fig. S3a), and this observation will be discussed in the context of other characterization observations later in the manuscript.

XRD patterns were obtained to understand the resulting crystal structure of the materials after different synthesis conditions, Fig. 3 shows the XRD patterns of the solution mixed and physically mixed samples fired at 500 °C for 6 h. The reference patterns of the potential lithiated TM oxide species are also shown at the bottom of Fig. 3. Oxide materials resulting from calcining the precursors in the absence of lithium salt were also obtained and analyzed, and the XRD patterns for these materials can be found in Supplementary Information, Fig. S4. The physically mixed sample fired with no LiOH added can be indexed with the patterns of Mn₂O₃ and NiO (PDF card codes being 04-007-0856 and 04-007-8202, respectively). This was consistent with the SEM images where Mn-dominant particles and Ni-dominant particles showed clear segregation, indicating that that the pure Mn precursor and pure Ni precursor formed pure Mn and Ni oxides, without much inter-diffusion of the two species. The peaks for these pure TM oxides also were present in the XRD pattern of the lithiated physically mixed sample (P-500-6, Fig. 3); the two most intense peaks: $2\theta =$ 33.1° and $2\theta = 43.4$ °, were consistent with Mn₂O₃ and NiO, respectively. Other peaks which appeared in the pattern were consistent with the patterns of LiMn₂O₄ and LiNiO₂ (PDF card numbers being 00-053-0830 and 00-062-0468, respectively). This observation was consistent with Li diffusing into the individual pure TM particles and converting some of the Ni and Mn oxides into lithiated oxides of Ni and Mn. LMNO structure may also have formed to an extent, but it

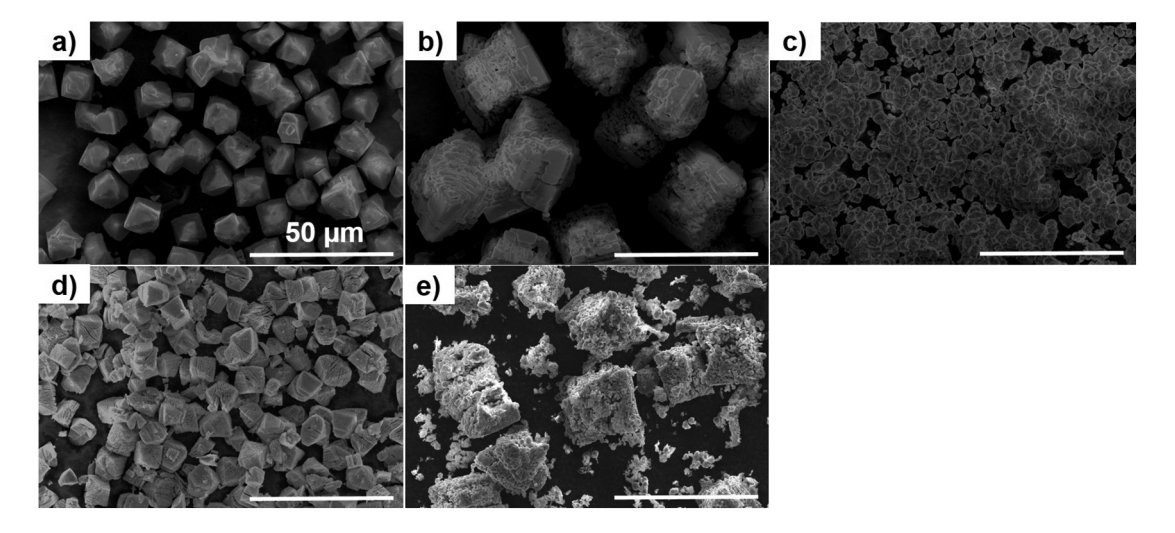


Fig. 1. SEM images of oxalate precursor particles a) $Mn_{0.74}Ni_{0.26}C_2O_4 \cdot 2H_2O$, b) $MnC_2O_4 \cdot 2H_2O$, c) $NiC_2O_4 \cdot 2H_2O$; and calcined oxide particles of the d) solution mixed sample fired at 850 °C for 6 h (P-850-6). Scale bars all correspond to 50 μ m.

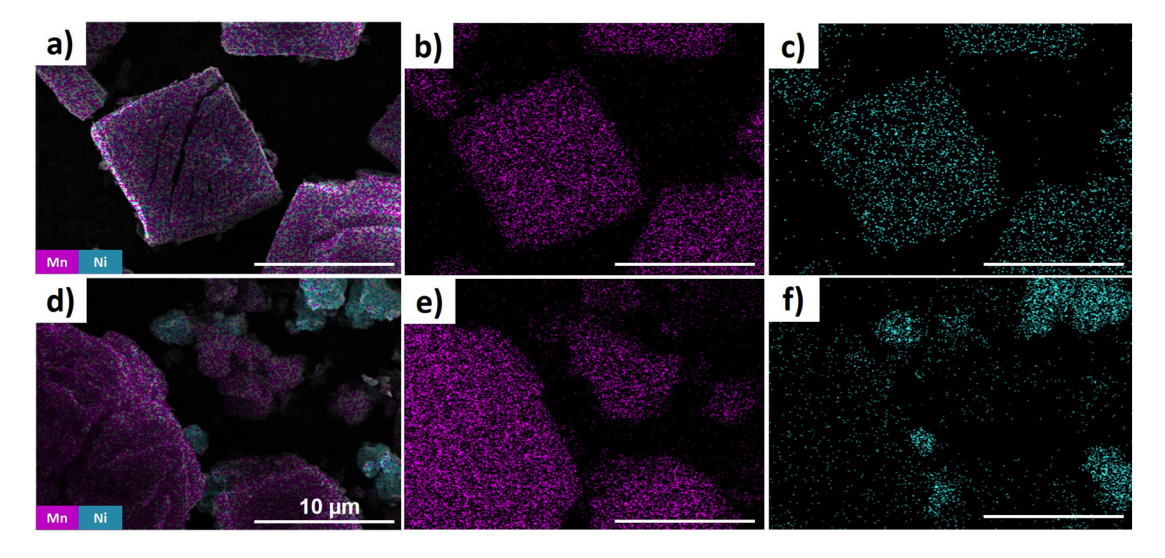


Fig. 2. EDS elemental compositional maps of a) solution mixed sample fired at 500 °C for 6 h (S-500-6 particles). EDS maps of the same region as a) with individual maps of only b) Mn and c) Ni. EDS elemental compositional maps of d) physically mixed sample fired at 500 °C for 6 h (P-500-6 particles). EDS maps are also shown of the same region as d) with individual maps for e) Mn and f) Ni. For all images, magenta corresponds to Mn and blue corresponds to Ni. All scale bars correspond to 10 μm.

was difficult to confirm the presence of LMNO directly from the XRD due to the overlap between LMNO and the pure transition metal lithiated oxide peaks [39]. The failure to form detectable amounts of target LMNO material for the physical mixture can be explained by the much greater distance between Mn and Ni TM ions when isolated in their particle domains, which made inter-diffusion of TM ions difficult. The XRD pattern of the S-500-6 sample, in contrast, exhibited intense peaks that were consistent with LMNO structures; and any peaks not consistent with LMNO were in line with those of the LiOH-free calcined control sample, and aligned well with the peaks from MnNiO₃ (PDF card number 04-002-0893, peaks at $2\theta = 24.8$, 36.6, and 50.8°) and Mn₂O₃ (peaks at $2\theta = 33.6$ and 55.2°). These lithium-free oxide peaks were much weaker in the lithiated sample. Tiny amounts of LiMn₂O₄ or LiNiO₂ may also exist in the lithiated material structure due to the

P-500-6

LiMn₂O₄ 00-053-0830

LiNiO₂ 00-062-0468

LiMn_{1.5}Ni_{0.5}O₄ 00-063-0626

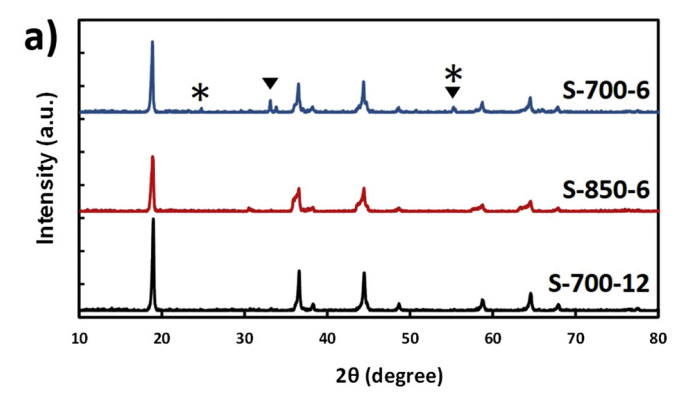
10 20 30 40 50 60 70 80

2θ (Degree)

Fig. 3. (Top) Powder XRD patterns and (bottom) the relevant reference patterns from the literature. Collected patterns from top to bottom correspond to physically mixed sample fired at 500 $^{\circ}$ C for 6 h (P-500-6, red) and solution mixed sample fired at 500 $^{\circ}$ C for 6 h (S-500-6, blue). The peak positions of the reference pattern of the potential lithiated TM oxide species are shown with their PDF card numbers at the bottom.

incomplete inter-diffusion between Mn and Ni ions, but it is difficult to distinguish these materials from the LMNO peaks in the pattern. The comparison between the XRD patterns of S-500-6 and P-500-6 samples was consistent with the picture that better mixing between Mn and Ni ions in the solution mixed precursor from coprecipitation reactions facilitated formation of final active materials with collocated Mn and Ni ions in the final oxide structures after firing even at the most moderate temperature. The isolation of TM ions in larger particles for the physically mixed sample rendered the inter-diffusion more challenging to complete due to the long diffusion distance, and thus there was likely less LMNO formed for an equivalent firing procedure.

The XRD patterns of both the solution mixed and physical mixed samples which were fired at 700 °C for 6 h (S-700-6 and P-700-6), 850 °C for 6 h (S-850-6 and P-850-6), and 700 °C for 12 h (S-700-12 and P-700-12) are shown in Fig. 4, with the solution mixed samples in Fig. 4a and physically mixed samples in Fig. 4b for comparison. The peaks corresponding to the unlithiated TM oxide species are also marked on the patterns with designated symbols. Within the solution mixed series, S-700-6 still exhibited peaks corresponding to MnNiO₃ and Mn₂O₃ (marked with a star and triangle, respectively) which had been observed in the S-500-6 sample (Fig. 3), whereas both S-700-12 and S-850-6 no longer contained these impurity peaks and all peaks were consistent with the LMNO spinel structure. The S-700-12 sample, however, had sharper peaks compared to S-850-6, which reflected higher crystallinity. The Scherrer formula, $d=\frac{K\lambda}{FWHM\cdot cos\theta}$, was used to estimate the crystal sizes of the calcined samples, where the shape factor was set equal to 0.9, λ was the x-ray wavelength (1.5406 Å), and FWHM is the full width at half maximum for a peak located at the given 2θ [40]. Using the intense peaks at $2\theta = 18.88^{\circ}$, the crystal sizes calculated for the three samples S-700-6, S-850-6, and S-700-12 were 31.8, 25.6, and 34.7 nm (listed in Table 1, which were consistent with other reports for similar materials [41]. (Note that these are estimates of the crystal grain size, which could be significantly smaller than the primary particle size in the calcined material.) These results indicated that firing the solution mixed sample at 700 °C for longer times facilitated crystal growth, while increasing the temperature from 700 °C to 850 °C may have stressed the material and crystal grains due to oxygen loss [42,43]. Comparing the XRD peaks of the physically mixed samples shown in Fig. 4b, P-700-6 peaks were at locations consistent with a mixture of both unlithiated TM oxides (Mn₂O₃ and NiO, marked with triangle and cube on Fig. 4b, respectively) and lithiated oxides



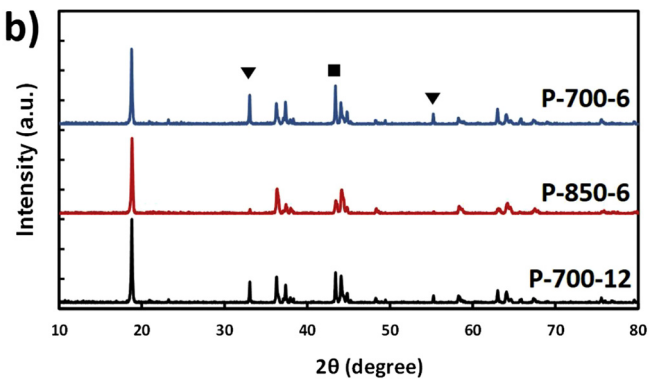


Fig. 4. XRD patterns of the a) solution mixed and b) physical mixed samples calcined at different target temperatures (700 °C or 850 °C, as labeled on the Figure) and for different holding times at the target temperature (6 or 12 h, as labeled). Peaks of unlithiated oxides are marked with special labels: Mn_2O_3 marked by triangle, NiO marked by cube, and MnNiO $_3$ marked by *.

(LiMn₂O₄ and LiNiO₂). P-850-6 and P-700-12 samples resulted in less intense unlithiated oxide peaks and stronger peaks from the lithiated species; particularly, the unlithiated oxides peaks in sample P-850-6 almost disappeared (the peaks at $2\theta = 33.6$ and 55.3° labeled in the pattern of P-700-6 which belong to Mn₂O₃). However, similar to the solution mixed samples, the physically mixed sample fired for a longer time at 700 °C exhibited improved crystallinity, as indicated by stronger peak intensity. The crystal sizes calculated using the Scherrer formula for P-700-6, and P-850-6, and P-700-12 are listed in Table 1. The slight increase of grain size of P-700-12 relative to P-700-6 and the decrease of grain size after increasing the temperature from 700 °C to 850 °C followed the same trend as in the solution mixed samples. These results indicated that for the physically mixed sample higher temperature firing resulted in greater conversion of the unlithiated oxide to lithiated oxide, while this improved conversion was accompanied lower crystallinity relative to a longer firing time at a lower temperature.

According to conventional theory of crystallization in solid phase, the major driving force for grain growth results from the reduction of

Table 1Grain sizes calculated using the Scherrer equation for samples fired using different target temperatures and hold times.

Calcination condition		Grain size (nm)			
		Solution mixed sample	Physically mixed sample		
500 °C	6 h	27.9	33.8		
700 °C	6 h	31.8	54.4		
	12 h	34.7	55.8		
	48 h	43.6	56.2		
850 °C	6 h	25.6	44.3		

the system energy from decreasing the grain boundary. The kinetic equation of grain growth can be given by [44]:

$$d^n - d_0^n = kt (1)$$

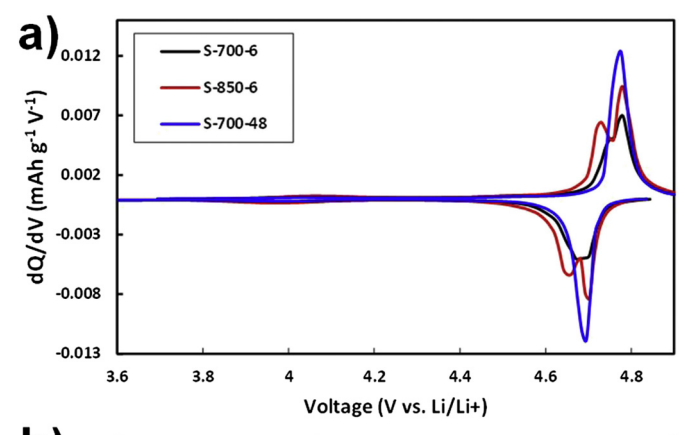
where d is the average grain size from either calculation or experimental analysis, d_0 is the initial grain size, n is the scaling exponent, and t is the time that a material is held at a given temperature where grain growth is occurring. In the equation, k is a temperature dependent constant which follows Arrhenius scaling, $k = Ae^{-E/RT}$. Assuming the initial grain size, d_0 , is far less than the grain size after calcination, d, the equation can be rearranged as:

$$\ln d = \frac{1}{n} \left(\ln t + \ln A - \frac{E}{RT} \right) \tag{2}$$

where for Eq. (2) there is a linear relationship between $\ln d$ and $\ln t$. The plot $\ln d$ vs. $\ln t$ using the samples fired at 700 °C for 6 h, 12 h, and 48 h for both the solution mixed and physically mixed samples is shown in Supplementary Information, Fig. S5. A linear least-squares fit for the solution mixed sample data resulted in a R^2 of 0.996 and a calculated n value equal to 6.5, and this n value is within the range of typical observations for crystal growth [44]. The fitting of the data from the physically mixed samples gives a R^2 of 0.75 and n of 74.6, which indicates both a poor fit of a linear function and an unreasonably high value for n to reflect the grain growth behavior – possibly indicating that the grains were not growing at these conditions, at least within the resolution of the Scherrer technique. In summary, the solution mixed precursor materials when fired to 700 °C had steady increases in grain size as the dwell time increased, while the physically mixed precursors had very similar grain sizes for all holding times.

Contrary to the observations of increasing the holding time, increasing the temperature of both solution mixed and physically mixed materials did not result in increased grain sizes. The calculated grain size decreased after increasing the temperature from 700 °C to 850 °C for both cases. One possible cause for the grain size reduction at 850 °C, as mentioned earlier, could have been because LMNO and other Mn spinel materials are known to undergo oxygen loss at this high temperature [42,43] and the loss of oxygen from the structure may have negatively impacted the grain growth and resulting sizes. Consistent with previous reports [43], oxygen loss would be expected to coincide with the formation of rock-salt phase within the material, and we speculate that the impurity rock-salt phase may inhibit growth of the spinel grains. Further support for oxygen loss at elevated calcination temperatures was provided by comparing the XRD peaks for the solution mixed samples fired at 700 °C and 850 °C (S-850-6 compared to both S-700-6 and S-700-12 in Fig. 4a). Note that for the sample fired to 850 °C the XRD peaks corresponding to the rock-salt impurity phase at $2\theta = 37.6^{\circ}$, 43.7°, and 63.5° were observed, suggesting that the higher temperature facilitated oxygen release and impurity rock-salt formation. We also note that the calculated grain sizes of the physically mixed samples were larger than those of the solution mixed samples fired under the same condition. This may have been due to the initially high segregation of the Mn and Ni in the physically mixed samples, where the highly separated Mn and Ni ions quickly formed very pure regions of Mn oxides and Ni oxides which were of higher initial phase purity compared to the mixed Mn/Ni oxides for the solution mixed samples.

These differences observed in transition metal distribution and crystal structure for final calcined materials resulting from solution versus physically mixed precursors suggested that the resulting materials would also have significantly different electrochemical properties. Fig. 5 shows the dQ/dV curves of the solution mixed (Fig. 5a) and physical mixed (Fig. 5b) LMNO samples, where the LMNO material was used as the active material in a composite cathode which was paired with a lithium metal anode. The firing conditions were 700 °C for 6 h, 700 °C for 48 h, and 850 °C for 6 h – this enabled comparison of the impact of



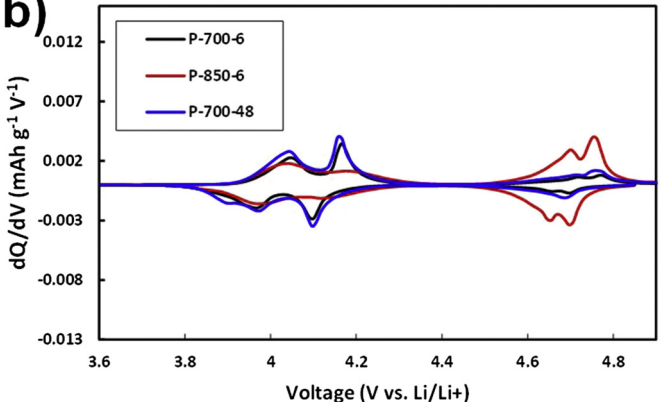


Fig. 5. dQ/dV plots from coin cells using a) solution mixed and b) physically mixed LMNO samples as the cathode active materials paired with lithium metal anodes. dQ/dV was collected from the 4th cycle, and each cell was charged and discharged at a rate of C/10 in a voltage window between 3.6 and 4.9 V (vs. Li/Li^+).

firing time versus firing temperature on electrochemical properties of the materials. Consistent with the observation of only LMNO-type peaks for the solution mixed samples processed using firing temperatures higher than 700 °C, the solution mixed samples all show clear dQ/dV peaks in the high voltage range (4.6–4.8 V vs. Li/Li⁺) consistent with LMNO high voltage spinel (Fig. 5a) [17]. Small peaks in 3.9-4.1 V range were also observed. The lower voltage capacity may come from either existing LiMn₂O₄ or LiNiO₂ in the structure or some fraction of Mn ions in the LMNO structure being reduced from Mn⁴⁺ to Mn³⁺ during synthesis [39]. The total capacities, and capacities separated by the high voltage (4.4-4.9 V) and low voltage (3.9-4.4 V) ranges, are listed in Table 2. Compared to S-700-6, both S-850-6 and S-700-48 had higher capacities in the high voltage range; meanwhile the low voltage capacities of S-850-6 and S-700-48 were both less than that of S-700-6. This means higher temperature and longer time both facilitated improved inter-diffusion of Mn and Ni ions, and the more complete formation of the target high voltage LMNO structure. The slightly higher low voltage capacity of sample S-850-6 compared to S-700-48 suggested partial reduction of some Mn⁴⁺ to Mn³⁺ after firing under 850 °C, which would be consistent with oxygen loss from the material at this high temperature [42,43]. Two separate peaks appear in the high voltage range in the profiles of S-700-6 and S-850-6; the S-700-48 sample, however, had a dominant higher voltage peak while the other peak at slightly lower voltage disappeared, which may have resulted from a larger ordered spinel phase domain in the LMNO structure [45].

There were also clear differences in electrochemical properties for the physically mixed samples (Fig. 5b). All of the physically mixed samples had much lower total capacity and capacity in the high voltage range, indicating the initial segregation of the Mn and Ni significantly hindered the formation of the high voltage spinel phase which requires significant Mn and Ni intermixing at local levels [45,46]. The P-700-6 sample showed two clear reversible peaks of Mn³⁺/Mn⁴⁺ redox activity in the range of 4.1 V vs. Li/Li⁺ [47]. We note there were very small peaks in the high voltage range consistent with Ni²⁺/Ni⁴⁺ redox couples from a high voltage spinel structure [17], but the low capacity in this range indicated the conversion of the material to the high voltage spinel phase was minimal. The corresponding low voltage capacity and high voltage capacity were 57.4 and 12.1 mAh/g for the sample. In comparison, the P-850-6 sample had higher magnitude peaks and increased capacity in the high voltage range, which was accompanied by reductions in intensity and total capacity of the low voltage peaks; the high voltage capacity increased from 12.1 mAh/g to 52.2 mAh/g. The change in the distribution of electrochemical activity was consistent with the increased temperature facilitating increased inter-diffusion of the two transition metal ions, and thus the formation of new phases (high voltage LMNO spinel) in the solid samples. In contrast, the P-700-48 sample had no significant changes in dQ/dV profile relative to the P-700-6 sample, which indicated that the higher temperature was needed to facilitate the diffusion of the highly segregated TMs, and that increased time at 700 °C was not sufficient to improve the formation of the high voltage LMNO spinel phase.

We note here that the total electrochemical capacity even for the solution mixed materials used in this study was <110 mAh/g. The goal was to compare, for identical processing after mixing with a lithium salt, the relative impact of the method of mixing the transition metals on the resulting properties of the final materials. Thus, the LMNO materials were not explicitly optimized for electrochemical performance. Due to the focus of this manuscript on the processing-property relationships as opposed to electrochemical performance optimization, these materials did not reach the 120–130 mAh/g reported in the literature for LMNO materials [46,48–50].

3.2. Model of diffusion-controlled solid reaction

Using the simplifying assumption that the precursor particles were all spheres, a model was applied to describe the ion diffusion and conversion of the particles to the desired LMNO phase during the solid reaction process initiated at the particle surface [51,52]. While assuming the particles were spheres introduced inaccuracy into the model results, we note that the secondary particles were octahedral and did not have significant differences in the lengths from the center to any of the edges. Also, this analysis was meant to determine diffusion times for comparative analysis, and thus the sphere radii were used for relative comparison between calcination conditions. The schematic of the

Table 2Total electrochemical gravimetric capacities, capacities within high voltage and low voltage ranges, and the calculated material amounts from the electrochemical profiles.

Sample mixing types	Sample names	Total capacity (mAh/g)	Low voltage (3.9–4.4 V) capacity (mAh/g)	High voltage (4.4–4.9 V) capacity (mAh/g)	Calculated LMO amount (g/g)	Calculated LMNO amount (g/g)
Solution mixed samples	S-700-6	99.3	18.5	80.8	0.12	0.55
	S-850-6	109.4	15.5	93.8	0.10	0.64
	S-700-48	103.7	12.6	91.2	0.08	0.62
Physically mixed samples	P-700-6	69.5	57.5	12.1	0.39	0.08
	P-850-6	103.4	51.2	52.2	0.34	0.36
	P-700-48	81.5	64.8	16.7	0.44	0.11

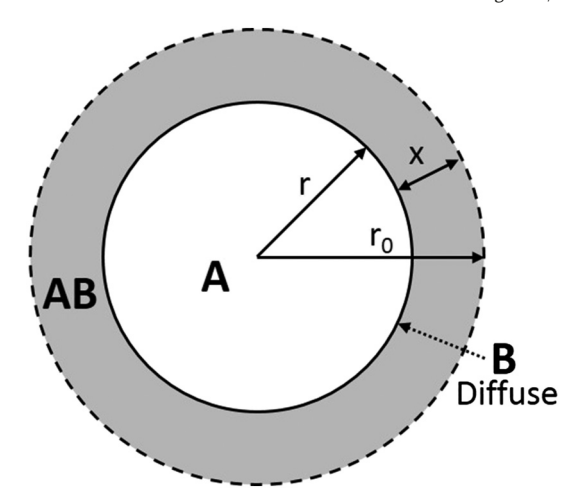


Fig. 6. Schematic for the model for diffusion-controlled solid reaction into a spherical particle, where A is the initial phase and B is the diffusing species which results in the formation of phase AB.

model is shown in Fig. 6. The initial solid component was represented as phase A with original radius r_0 . The diffusing species was represented as B and could be in either solid or liquid phase. The phase AB was the layer of the solid product that built up as species B diffused through the layer and reacted with A at the interface between A and AB. The growth of AB was assumed to be diffusion controlled, and at time t the product layer had a thickness of x, which resulted in the sphere of remaining phase A having a radius r, where t0 - t1. The resulting volume of remaining A at time t1 was given by:

$$V = \frac{4}{3}\pi (r_0 - x)^3. \tag{3}$$

Therefore, for a converted fraction of A, α , the unreacted fraction of component A was

$$(1-\alpha) = \frac{\frac{4}{3}\pi(r_o - x)^3}{\frac{4}{3}\pi r_o^3} = \frac{(r_o - x)^3}{r_o^3}.$$
 (4)

Rearranging Eq. (4) results in an expression for x:

$$x = r_o \left(1 - (1 - \alpha)^{1/3} \right). \tag{5}$$

The above manipulation also assumed that the volume change of the product AB compared to species A was negligible. For the assumption that the diffusion across the product layer was the rate determining step, the parabolic diffusion law was also applied where the progression of product formation was proportional to the square root of time [52]:

$$x^2 = 2DV_m C_0 t = k_1 t, \tag{6}$$

where D was the diffusion coefficient of species B, V_m was the volume of product AB formed from per mole of species B, and C_0 was the concentration of B outside the sphere; therefore $k_1 = 2DV_mC_0$, was a constant used for convenience.

Table 3Parameters used for diffusion-controlled solid reactions forming LMNO analysis [53,55].

 $D_o (m^2/S)$ $D_{850^{\circ}\text{C}}\,(\,m^2/\text{S}\,)$ E_o (eV) $D_{700^{\circ}C}\,(m^2/S)$ $V_m \, (m^3/mol)$ $C_0 \, (mol/m^3)$ 3.60×10^{-10} 7.11×10^{-10} 4.12×10^{-5} Li+ 1.7×10^{-7} 0.53 6.10×10^{4} 2.40×10^{-20} 6.79×10^{-19} 8.23×10^{-5} Ni^{2+} 1.8×10^{-9} 9.52×10^4 2.10

Combining Eqs. (5) and (6) gives the relationship between reaction fraction and time:

$$\left(1 - (1 - \alpha)^{1/3}\right)^2 = k't,$$
 (7)

where $k' = \frac{k_1}{r_0^2} = \frac{2DV_mC_0}{r_0^2}$. Therefore, with estimates for the diffusion coefficient of the penetrating species at a given temperature and the original particle size, the reaction fraction was calculated for a given firing time.

3.2.1. Solution mixed samples

For the case of solution mixed samples, Mn and Ni ions were assumed to be homogeneously distributed within the precursor particles and lithium ions were diffusing across the product layer and reacting with the unlithiated TM oxide to form the product LMNO. In other words, lithium ions were the penetrating species B in Fig. 6 and the sphere of A was a mixture of all the unlithiated TM oxides. AB in the schematic was the final product LMNO. The dependence of lithium ion diffusion coefficient through spinel structure was represented using the Arrhenius equation:

$$D(T) = D_0 e^{-E_0/kT} \tag{8}$$

where D_0 was the pre-exponential factor; E_0 was the diffusion activation energy; k was the Boltzmann constant which was equal to 8.617 \times 10⁻⁵eV/K and T was the temperature in units of Kelvin. The preexponential factor and activation energy for lithium diffusion were taken from the literature and listed in Table 3. The original parameters were obtained for lithium ion diffusion through layered structures containing elements Mn, Ni, and Co, but provide a rough estimation for the materials in this study [53]. The diffusion coefficients at 700 °C and 850 °C were thus calculated using Eq. (8) and the values are listed in Table 3, along with the other two parameters needed to calculate k' in Eq. (7). Further details for calculating these parameters can be found in the Supplementary Information. Using the secondary particle size measured from SEM images, the original particle size $r_0 = 1.02 \times 10^{-5}$ m, and thus value k' of lithium ions diffusion controlled reaction process in Eq. (7) was obtained as $14.8 \, \mathrm{S}^{-1}$. Substituting the parameter in Eq. (7), we calculated that at 700 °C complete conversion to LMNO, corresponding to a reaction fraction of 1, would require only 0.068 s. The influence of the choice of original particle size will be discussed in further detail later, but has little influence in the current case because the lithium diffuses very quickly at the elevated temperature. The pores that develop in the secondary particles during calcination likely makes this timescale estimate based purely on lithium diffusion an

Even though the calculation above indicated that lithium diffusion was fast and should be complete within a second, the experimental LMNO amount in sample S-700-6 calculated based on the high voltage capacity during discharge, was only 0.55 g per gram of the sample (equivalently a conversion of only 0.61, the conversion calculation details can be found in Supplementary Information). While part of this lack of conversion was because spinel materials generally do not have complete delithiation during charge [43], the conversion of 0.61 suggested that lithium ion diffusion does not explicitly determine the conversion to the LMNO phase. We next considered that the interdiffusion of Mn and Ni ions could be the process that limits the formation of LMNO high voltage spinel. To simplify the situation, we used

the same diffusion controlled reaction analysis and defined nickel ions as the penetrating species as in Fig. 6 and manganese ions along with other compounds (Li, O) as the static species in a fixed domain in phase A, although in reality the manganese ions also diffuse into nickel dominant regions during the inter-diffusion process [54]. Nickel was chosen as the penetrating species because according to a previous study it has greater diffusivity [55]. The diffusion coefficient parameters as well as other parameters for this case were also found in the literature [55] and are listed in Table 3. Given that at 700 °C for 6 h, the reaction fraction was 0.61, via substitution into Eq. (7) the original domain size was determined to be 386 nm. This large value relative to the atomic scale assumed for coprecipitation can be partially explained by the non-stoichiometry and impurity of the final active material - which hindered the full extraction of capacity and would result in a larger calculated domain size. By only considering diffusion of a single species, the energy associated with formation of the desired phase, as well as the formation and distribution of metastable phases and regions, has been ignored. These factors are essential for more accurate prediction of the reaction process during the calcination step and need further study. We do note that while the coprecipitation certainly resulted in improved local mixing of the TMs, it may not be truly atomic level mixing as has been described [56]. Further investigation into quantifying the extent of local mixing of TMs in the precursor will be the subject of future studies.

3.2.2. Physically mixed samples

In the case of physically mixed samples, the same calculation technique was applied as discussed above. Similar to the solution mixed samples, the lithium ion diffusion was estimated to be extremely fast due to the low activation energy and especially the high temperature applied, which would have completed the reaction in this idealized case within 0.1 s, resulting in lithiated products LiMn₂O₄ and LiNiO₂. Although the operating voltage for the Mn³⁺/Mn⁴⁺ redox couple in LiMn₂O₄ and the Ni³⁺/Ni⁴⁺ redox couple in LiNiO₂ both have capacity close to 4.1 V vs. Li/Li^+ , and both could contribute to the low voltage capacity in the discharge profiles, for simplification of the materials comparison all the low voltage capacity was assigned to Mn³⁺/Mn⁴⁺ in LiMn₂O₄. The resulting calculated LMO was 0.39 g per gram of material for sample S-700-6, as given in Table 2 (all the other samples can also be found in the table). The sum of the LMO amount plus the LMNO amount, based on the low voltage and high voltage capacities, was still less than unity. This indicated that all of the lithium could not be extracted from the active material. As stated above, we assumed that the nickel ions were the penetrating species diffusing from the NiO to form the product LMNO layer via reaction with lithiated manganese oxide LMO (refer to the schematic in Fig. 6). As in the case of the solution mixed samples, we used the secondary particle size from SEM image analysis as the original spherical size r₀ and calculated the reaction fraction as a result of nickel ion diffusion for each physically mixed sample. The calculated values for samples P-700-6, P-850-6, and P-700-48 were 0.013, 0.21, and 0.038. The amount of final product LMNO per gram of the sample can then be calculated from the reaction fractions and the values are 0.01, 0.17, and 0.03 g/g. Further details on these calculations can be found in the Supplementary Information. In order to see the influence of particle size on the reaction fraction for the three samples, we also used the primary particle size estimated from the SEM images as the original particle size (~1 µm) and used this value as the input for the calculation, resulting in reaction fractions increasing to 0.25, 0.86, and 0.59, and the calculated LMNO amounts were 0.21, 0.83, and 0.53 g/g for sample P-700-6, P-850-6, and P-700-48 respectively. For better comparison, the LMNO amounts calculated using either secondary or primary particle sizes are listed in Table 4 and are compared to the LMNO amounts determined from electrochemical data from Table 2. It can be seen that the electrochemically determined LMNO amounts were in between the two values for particle sizes. Though there were many simplifications to the calculation approach used, these results suggested that the average original particle size was between the primary and secondary particle sizes, which would be reasonable given that the secondary particle precursors have pores that open up during calcination and decomposition of the oxalate, and also that the primary particles fuse with each other making a network structure within the secondary particle as observed in the SEM images (Fig. S6) – both of these phenomena result in effective particle sizes between the observed primary and secondary particle length scales.

Comparing the reaction fractions calculated by using the secondary particle size between the three samples, we can see that increasing the firing temperature from 700 °C to 850 °C increased the reaction fraction as much as 16 times while expanding the firing time from 6 h to 48 h at 700 °C only increased the conversion as much as 3 times, which were consistent with the XRD analyses. This observation was attributed to the large activation energy of TM ion diffusion which makes the diffusion coefficient highly sensitive to temperature, in particular the value of D_{850°C} was more than one order of magnitude larger than D_{700°C} (Table 3). Thus, for poorly mixed samples greater conversion to LMNO can be achieved with higher firing temperature as opposed to extended firing time at lower temperature – the P-850-6 sample had much more high voltage LMNO than the P-700-48 sample. In addition, the reaction fractions calculated from using the primary particle size decreased the gaps between sample P-850-6 and P-700-6, which indicated decreasing the initial particle size can aid in overcoming the diffusive intermixing limitation and promote lower temperature and/or calcination time to higher conversion of LMNO, although P-850-6 still resulted in a higher overall conversion.

4. Conclusion

In this work we provided quantitative evidence that coprecipitation facilitates high levels of local mixing within precursor particles, and showed via different calcination procedures the advantages of local mixing from coprecipitation relative to physical mixing of individual single component precursors. Evidence of the improved mixing of the transition metals was provided by EDS, XRD, and electrochemical analysis. A simple diffusion limited reaction model suggested that the diffusion of Li⁺ was not limiting the conversion of solution mixed or physically mixed precursor materials to the desired final material, and that the conversion was largely limited by the diffusion of transition metal species. The better local mixing of transition metal ions after coprecipitation reaction renders the synthesis process less energy consuming for conversion to final active material.

Table 4LMNO amounts in the physically mixed samples calculated using different particle sizes and determined from electrochemical data.

Sample	Reaction fraction α		LMNO amounts (g/g of sample)		
	Calculated using secondary particle size	Calculated using primary particle size	Calculated using secondary particle size	Calculated using primary particle size	Electrochemically determined
P-700-6	0.013	0.25	0.01	0.21	0.08
P-850-6	0.21	0.86	0.17	0.83	0.36
P-700-48	0.038	0.59	0.03	0.53	0.11

Acknowledgments

This work was supported by the National Science Foundation, through grant awards CBET-1652488 and ECCS-1405134. The authors also thank Prof. Geoff Geise for use of their lab's TGA instrument.

Appendix A. Supplementary data

Supplementary data to this article can be found online at https://doi.org/10.1016/j.powtec.2018.05.020.

References

- J.B. Goodenough, K.-S.S. Park, The Li-ion rechargeable battery: a perspective, J. Am. Chem. Soc. 135 (2013) 1167–1176, https://doi.org/10.1021/ja3091438.
- [2] J. Wang, X. Yao, X. Zhou, Z. Liu, Synthesis and electrochemical properties of layered lithium transition metal oxides, J. Mater. Chem. 21 (2011) 2544–2549, https://doi. org/10.1039/C0IM03388I.
- [3] C.M. Julien, A. Mauger, Review of 5-V electrodes for Li-ion batteries: status and trends, Ionics (Kiel). 19 (2013) 951–988, https://doi.org/10.1007/s11581-013-0913-2
- [4] H. Li, Q. Xu, X.-X. Shi, D.-W. Song, L.-Q. Zhang, Electrochemical performance of LiNi0.5Mn0.5O₂ with different synthesis methods, Rare Metals 34 (2015) 580–585, https://doi.org/10.1007/s12598-013-0088-z.
- [5] W. Ren, Y. Zhao, X. Hu, M. Xia, Preparation-microstructure-performance relationship of Li-rich transition metal oxides microspheres as cathode materials for lithium ion batteries, Electrochim. Acta 191 (2016) 491–499, https://doi.org/10.1016/j. electacta.2016.01.089.
- [6] L. Shen, H. Li, E. Uchaker, X. Zhang, G. Cao, General strategy for designing core–shell nanostructured materials for high-power lithium ion batteries, Nano Lett. 12 (2012) 5673–5678, https://doi.org/10.1021/nl302854j.
- [7] X. Huang, Y. You, Y. Ren, H. Wang, Y. Chen, X. Ding, B. Liu, S. Zhou, F. Chu, Spray drying-assisted synthesis of hollow spherical Li₂FeSiO₄/C particles with high performance for Li-ion batteries, Solid State Ionics 278 (2015) 203–208, https://doi.org/10.1016/j.ssi.2015.06.019.
- [8] F. Wu, Z. Wang, Y. Su, Y. Guan, Y. Jin, N. Yan, J. Tian, L. Bao, S. Chen, Synthesis and characterization of hollow spherical cathode Li1.2Mn0.54Ni0.13Co0.13O₂ assembled with nanostructured particles via homogeneous precipitation-hydrothermal synthesis, J. Power Sources 267 (2014) 337–346, https://doi.org/10.1016/j.jpowsour.2014.05.097.
- [9] J.S. Park, X. Meng, J.W. Elam, S. Hao, C. Wolverton, C. Kim, J. Cabana, Ultrathin lithium-ion conducting coatings for increased interfacial stability in high voltage lithium-ion batteries, Chem. Mater. 26 (2014) 3128–3134, https://doi.org/10. 1021/cm500512n.
- [10] S. Zhang, C. Deng, B.L. Fu, S.Y. Yang, L. Ma, Synthetic optimization of spherical Li[Ni1/3Mn1/3Co1/3]O₂ prepared by a carbonate co-precipitation method, Powder Technol. 198 (2010) 373–380, https://doi.org/10.1016/j.powtec.2009.12.002.
- [11] G.M. Koenig, I. Belharouak, H. Deng, Y.-K. Sun, K. Amine, Composition-tailored synthesis of gradient transition metal precursor particles for lithium-ion battery cathode materials, Chem. Mater. 23 (2011) 1954–1963, https://doi.org/10.1021/ cm/200688c
- [12] G.T.-K. Fey, C.-Z. Lu, T.P. Kumar, Preparation and electrochemical properties of high-voltage cathode materials, LiMyNi0.5—yMn1.504 (M = Fe, Cu, Al, Mg; y = 0.0–0.4), J. Power Sources 115 (2003) 332–345, https://doi.org/10.1016/S0378-7753(03) 00010-7.
- [13] I. Belharouak, G.M. Koenig, K. Amine, Electrochemistry and safety of Li₄Ti₅O₁₂ and graphite anodes paired with LiMn₂O₄ for hybrid electric vehicle Li-ion battery applications, J. Power Sources 196 (2011) 10344–10350, https://doi.org/10.1016/j.jpowsour.2011.08.079.
- [14] L. Wang, D. Chen, J. Wang, G. Liu, W. Wu, G. Liang, Synthesis of LiNi0.5Mn1.5O4cathode material with improved electrochemical performances through a modified solid-state method, Powder Technol. 292 (2016) 203–209, https://doi.org/10.1016/j.powtec.2016.02.002.
- [15] Z., Peng, C., Wan, C., Jiang, Synthesis by sol–gel process and characterization of LiCoO₂ cathode materials, J. Power Sources 72 (1998) 215–220, https://doi.org/10. 1016/S0378-7753(97)02689-X.
- [16] R. Thirunakaran, G.H. Lew, W.S. Yoon, Cerotic acid assisted sol-gel synthesis and electrochemical performance of double doped spinels (LiCrxMgyMn2-x-yO4) as cathode materials for lithium rechargeable batteries, Powder Technol. 301 (2016) 197–210, https://doi.org/10.1016/j.powtec.2016.05.064.
- [17] K. Amine, H. Tukamoto, H. Yasuda, Y. Fujita, Preparation and electrochemical investigation of LiMn₂–xMexO₄ (Me: Ni, Fe, and x = 0.5, 1) cathode materials for secondary lithium batteries, J. Power Sources 68 (1997) 604–608, https://doi.org/ 10.1016/S0378-7753(96)02590-6.
- [18] F. Wu, H. Lu, Y. Su, N. Li, L. Bao, S. Chen, Preparation and electrochemical performance of Li-rich layered cathode material, Li[Ni0.2Li0.2Mn0.6]O₂, for lithium-ion batteries, J. Appl. Electrochem. 40 (2010) 783–789, https://doi.org/10.1007/s10800-009-0057-2.
- [19] I. Taniguchi, N. Fukuda, M. Konarova, Synthesis of spherical LiMn₂O₄ microparticles by a combination of spray pyrolysis and drying method, Powder Technol. 181 (2008) 228–236, https://doi.org/10.1016/j.powtec.2007.05.011.

- [20] M. Konarova, I. Taniguchi, Preparation of carbon coated LiFePO4 by a combination of spray pyrolysis with planetary ball-milling followed by heat treatment and their electrochemical properties, Powder Technol. 191 (2009) 111–116, https://doi.org/ 10.1016/i.powtec.2008.09.013.
- [21] P. Yue, Z. Wang, W. Peng, L. Li, W. Chen, H. Guo, X. Li, Spray-drying synthesized LiNi0.6Co0.2Mn0.2O2 and its electrochemical performance as cathode materials for lithium ion batteries, Powder Technol. 214 (2011) 279–282, https://doi.org/10. 1016/j.powtec.2011.08.022.
- [22] D. Liu, J. Han, J.B. Goodenough, Structure, morphology, and cathode performance of Li1-x[Ni0.5Mn1.5]O4 prepared by coprecipitation with oxalic acid, J. Power Sources 195 (2010) 2918–2923, https://doi.org/10.1016/j.jpowsour.2009.11.024.
- [23] J.P. Robinson, G.M. Koenig, Tuning solution chemistry for morphology control of lithium-ion battery precursor particles, Powder Technol. 284 (2015) 225–230, https://doi.org/10.1016/j.powtec.2015.06.070.
- [24] A. Van Bomme, J.R. Dahn, Analysis of the growth mechanism of coprecipitated spherical and dense nickel, manganese, and cobalt-containing hydroxides in the presence of aqueous ammonia, Chem. Mater. 21 (2009) 1500–1503, https://doi. org/10.1021/cm803144d.
- [25] K.-M. Nam, H.-J. Kim, D.-H. Kang, Y.-S. Kim, S.-W. Song, Ammonia-free coprecipitation synthesis of a Ni-Co-Mn hydroxide precursor for high-performance battery cathode materials, Green Chem. 17 (2015) 1127–1135, https://doi.org/10.1039/C4GC01898B.
- [26] Q. Zhong, A. Bonakdarpour, M. Zhang, Y. Gao, J.R. Dahn, Synthesis and electrochemistry of LiNixMn₂-xO₄, J. Electrochem. Soc. 144 (1997) 205–213, https://doi.org/10.1149/1.1837386.
- [27] L. Wang, H. Li, X. Huang, E. Baudrin, A comparative study of Fd-3m and P4332 "LiNi0.5Mn1.5O4", Solid State Ionics 193 (2011) 32–38, https://doi.org/10.1016/j. ssi 2011 04 007
- [28] D. Wang, I. Belharouak, G. Zhou, K. Amine, Synthesis of lithium and manganese-rich cathode materials via an oxalate co-precipitation method, J. Electrochem. Soc. 160 (2013) A3108–A3112, https://doi.org/10.1149/2.016305jes.
- [29] A. Angermann, J. Töpfer, Synthesis of nanocrystalline Mn-Zn ferrite powders through thermolysis of mixed oxalates, Ceram. Int. 37 (2011) 995–1002, https://doi.org/10. 1016/j.ceramint.2010.11.019.
- [30] H. Dong, G.M. Koenig Jr, Compositional control of precipitate precursors for lithiumion battery active materials: role of solution equilibrium and precipitation rate, J. Mater. Chem. A 5 (2017) 13785–13798, https://doi.org/10.1039/C7TA03653A.
- [31] M.C. López, J.L. Tirado, C. Pérez Vicente, Structural and comparative electrochemical study of M(II) oxalates, M = Mn, Fe, Co, Ni, Cu, Zn, J. Power Sources 227 (2013) 65–71, https://doi.org/10.1016/j.jpowsour.2012.08.100.
- [32] N. Mancilla, V. Caliva, M.C. D'Antonio, A.C. González-Baró, E.J. Baran, Vibrational spectroscopic investigation of the hydrates of manganese(II) oxalate, J. Raman Spectrosc. 40 (2009) 915–920, https://doi.org/10.1002/jrs.2200.
- [33] S.-K. Hong, S.-I. Mho, I.-H. Yeo, Y. Kang, D.-W. Kim, Structural and electrochemical characteristics of morphology-controlled Li[Ni0.5Mn1.5]O4 cathodes, Electrochim. Acta 156 (2015) 29–37, https://doi.org/10.1016/j.electacta.2015.01.027.
- [34] X. Zhang, F. Cheng, K. Zhang, Y. Liang, S. Yang, J. Liang, J. Chen, Facile polymerassisted synthesis of LiNi0.5Mn1.504 with a hierarchical micro-nano structure and high rate capability, RSC Adv. 2 (2012) 5669, https://doi.org/10.1039/ c2ra20669b.
- [35] Q. Zhong, A. Bonakclarpour, M. Zhang, Y. Gao, J.R. Dahn, Synthesis and electrochemistry of LiNixMn₂-xO₄, J. Electrochem. Soc. 144 (1997) 205–213, https://doi.org/10. 1149/1.1837386.
- [36] J.-H. Kim, S.-T. Myung, C.S. Yoon, S.G. Kang, Y.-K. Sun, Comparative study of LiNi0.5Mn1.504-δ and LiNi0.5Mn1.504 cathodes having two crystallographic structures: Fd 3 m and P 4332, Chem. Mater. 16 (2004) 906–914, https://doi.org/10. 1021/cm035050s.
- [37] J. Topfer, J. Jung, Thermal decomposition of mixed crystals NixMn3-x(C2O4)3.6H2O, Thermochim. Acta 202 (1992) 281–289.
- [38] M.E. Brown, A.K. Galwey, Thermal decomposition of manganese(II) oxalate in vacuum and in oxygen, J. Chem. Soc. Faraday Trans. 1 Phys. Chem. Condens. Phases. 70 (1974) 1316–1324.
- [39] I. Belharouak, G.M. Koenig, J. Ma, D.P. Wang, K. Amine, Identification of LiNi0.5Mn1.504spinel in layered manganese enriched electrode materials, Electrochem. Commun. 13 (2011) 232–236, https://doi.org/10.1016/j.elecom. 2010.12.021.
- [40] R.B. Von Dreele, B.H. Toby, X-ray powder diffraction, Charact. Mater. (2012) 1340–1360, https://doi.org/10.1002/0471266965.
- [41] J.H. Kim, A. Huq, M. Chi, N.P.W. Pieczonka, E. Lee, C.A. Bridges, M.M. Tessema, A. Manthiram, K.A. Persson, B.R. Powell, Integrated nano-domains of disordered and ordered spinel phases in LiNi0.5Mn1.504 for li-ion batteries, Chem. Mater. 26 (2014) 4377–4386, https://doi.org/10.1021/cm501203r.
- [42] A. Manthiram, K. Chemelewski, E.-S. Lee, A perspective on the high-voltage LiMn1.5Ni0.504 spinel cathode for lithium-ion batteries, Energy Environ. Sci. 7 (2014) 1339, https://doi.org/10.1039/c3ee42981d.
- [43] J. Song, D.W. Shin, Y. Lu, C.D. Amos, A. Manthiram, J.B. Goodenough, Role of oxygen vacancies on the performance of Li[Ni0.5—xMn1.5+x]04 (x = 0, 0.05, and 0.08) spinel cathodes for Lithium-ion batteries, Chem. Mater. 24 (2012) 3101–3109.
- [44] X. Song, D. Liu, Y. Zhang, Y. Ding, M. Li, S. Wang, X. He, Y. Qu, Grain growth kinetics of SnO₂ nanocrystals synthesized by precipitation method, J. Wuhan Univ. Technol. Mater. Sci. Ed. 25 (2010) 929–934, https://doi.org/10.1007/s11595-010-0122-z.
- [45] E.S. Lee, K.W. Nam, E. Hu, A. Manthiram, Influence of cation ordering and lattice distortion on the charge-discharge behavior of LiMn 1.5Ni 0.5O 4 spinel between 5.0 and 2.0 v, Chem. Mater. 24 (2012) 3610–3620, https://doi.org/10.1021/cm3020836.
- [46] K.R. Chemelewski, E.S. Lee, W. Li, A. Manthiram, Factors influencing the electrochemical properties of high-voltage spinel cathodes: relative impact of morphology

- and cation ordering, Chem. Mater. 25 (2013) 2890–2897, https://doi.org/10.1021/cm401496k.
- [47] J.M. Tarascon, The spinel phase of $LiMn_2O_4$ as a cathode in secondary lithium cells, I. Electrochem. Soc. 138 (1991) 2859, https://doi.org/10.1149/1.2085330.
- [48] Y. Idemoto, H. Narai, N. Koura, Crystal structure and cathode performance dependence on oxygen content of LiMn1.5Ni0.5O4 as a cathode material for secondary lithium batteries, J. Power Sources 119–121 (2003) 125–129, https://doi.org/10.1016/S0378-7753(03)00140-X.
- [49] W. Luo, Effect of morphology on the physical and electrochemical properties of the high-voltage spinel cathode LiMn1.5Ni0.5O4, J. Alloys Compd. 636 (2015) 24–28, https://doi.org/10.1016/j.jallcom.2015.02.163.
- [50] K.R. Chemelewski, D.W. Shin, W. Li, A. Manthiram, Octahedral and truncated high-voltage spinel cathodes: the role of morphology and surface planes in electrochemical properties, J. Mater. Chem. A 1 (2013) 3347, https://doi.org/10.1039/c3ta00682d.
- [51] R.E. Carter, Kinetic model for solid-state reactions, J. Chem. Phys. 34 (1961) 2010–2015, https://doi.org/10.1063/1.1731812.

- [52] C.F. Dickinson, G.R. Heal, Solid-liquid diffusion controlled rate equations, Thermochim. Acta 340–341 (1999) 89–103, https://doi.org/10.1016/S0040-6031 (99)00256-7
- [53] S. Yang, B. Yan, J. Wu, L. Lu, K. Zeng, Temperature-dependent Lithium-ion diffusion and activation energy of Li1.2Co0.13Ni0.13Mn0.5402 thin-film cathode at nanoscale by using electrochemical strain microscopy, ACS Appl. Mater. Interfaces 9 (2017) 13999–14005, https://doi.org/10.1021/acsami.6b16321.
- [54] J. Li, R. Doig, J. Camardese, K. Plucknett, J.R. Dahn, Measurements of interdiffusion coefficients of transition metals in layered Li-Ni-Mn-Co oxide core-shell materials during sintering, Chem. Mater. 27 (2015) 7765–7773, https://doi.org/10.1021/acs. chemmater.5b03499.
- [55] B.J. Wuensch, T. Vasilos, Diffusion of transition metal ions in single-crystal MgO, J. Chem. Phys. 36 (1962) 2917, https://doi.org/10.1063/1.1732402.
- [56] D.G. Wickham, Solid-phase equilibria in the system NiO-Mn₂O₃-O₂, J. Inorg. Nucl. Chem. 26 (1964) 1369–1377.